Surface & Coatings Technology 222 (2013) 104–111

Contents lists available at SciVerse ScienceDirect

Surface & Coatings Technology

journal homepage: www.elsevier.com/locate/surfcoat

Ag^+ release and corrosion behavior of zirconium carbonitride coatings with silver nanoparticles for biomedical devices

S. Calderon V. [a,*], R. Escobar Galindo [b], J.C. Oliveira [c], A. Cavaleiro [c], S. Carvalho [a]

[a] Universidade do Minho, Dept. Física, Campus de Azurém, 4800-058 Guimarães, Portugal
[b] Instituto de Ciencia de Materiales de Madrid (ICMM—CSIC), Cantoblanco, 28049, Madrid, Spain
[c] SEG-CEMUC Mechanical Engineering Department, University of Coimbra, 3030-788 Coimbra, Portugal

ARTICLE INFO

Article history:
Received 24 January 2013
Accepted in revised form 12 February 2013
Available online 21 February 2013

Keywords:
Corrosion resistance
Potentiodynamic
ZrCN
GD-OES
ICP

ABSTRACT

Zirconium carbonitride coatings with silver nanoparticles were produced by DC unbalanced dual magnetron sputtering system, using two targets, Zr and Zr/Ag in an Ar, C_2H_2 and N_2 atmosphere. Stainless steel 316L and silicon (100) substrates were used for electrochemical and structural characterization, respectively. Silver was found to be well distributed throughout the coatings, maintaining the films' composition in depth, while its diffusion to the electrolyte decreases as immersion time increases, stopping its release after 7 to 8 days of immersion. Electrochemical characterization revealed very stable films that have improved base material, without any diminished corrosion resistance due to the silver content.

1. Introduction

Ti and Co alloys together with stainless steel have been extensively used in biomaterials. Stainless steel, for instance, has become strongly used for a wide range of applications since Ti osseointegration ability is undesirable. In addition, it has been proven that stainless steel 316L (SS316L), Ti alloys and CoCrMo alloys present similar wear rates, with friction coefficients between 0.34 and 0.58 with the lowest friction coefficient found for the SS316L [1], supporting the use of this material based on the cost–performance ratio. However, stainless steels are affected by localized corrosion in long-term applications due to aggressive biological environment [2], leading to a strong necessity of changing the material surface properties such as chemical stability, and mechanical and tribological properties in order to enable their use for such scenarios. Hence, surface modification of SS316L using $ZrC_{1-x}N_x$ coating to enhance corrosion resistance and add mechanical, tribological and biocompatible properties is a promissory field of study.

$ZrC_{1-x}N_x$ films are gaining special attention due to their proven wear resistance, hardness, thermal stability and corrosion resistance [3–9]. However, only few reports on $ZrC_{1-x}N_x$ composite films are available [2–4,6,7,9–14]. Hollstein et al. [11], for example, emphasized that $ZrC_{1-x}N_x$ layers ensure chemical stability in hydrogen peroxide compared with $TiC_{1-x}N_x$ thin films. It has also been mentioned that $ZrC_{1-x}N_x$ and ZrN reveal lower friction coefficients compared with TiN [12]. On the same basis, Larijani et al. [13] stated that despite the fact that $ZrC_{1-x}N_x$ films show slightly less hardness than TiCN, their corrosion resistance is improved.

Consequently, these materials are considered good candidates for biomaterial design and could be suitable in applications such as knee and hip prostheses since these devices are subjected to mechanical/wear solicitation under a corrosive environment. However, materials for biomedical applications must satisfy additional characteristics among which biocompatibility and antibacterial behavior must be emphasized. The latter property has been achieved by several authors by introducing silver nanoparticles with different sizes, geometries [15] and amounts [16] into materials such as DLC [17–22], Ti alloys [15,23–26] and different types of polymers [27], obtaining considerable good antibacterial effect. Nevertheless, the design of a more controlled silver release without compromising the multifunctional properties and the antibacterial effect's durability is still in development.

As a result, the present work aims to report the production of $ZrC_{1-x}N_x$ films with embedded silver nanoparticles deposited onto SS316L by dual magnetron sputtering and evaluates silver the ion release and corrosion resistance of this system. Nevertheless, the physical, mechanical and chemical properties of zirconium carbonitride films prepared by magnetron sputtering depend on several parameters such as nitrogen and carbon content, deposition rate and substrate holder rotation [28]; a systematic study about the stability of these variables along the substrate holder was performed.

2. Experimental details

Films were deposited using a dual unbalanced magnetron sputtering system having a 99.8% Zr target and a modified Zr target with Ag pellets

* Corresponding author. Tel.: +351 253510175x517465; fax: +351 253510461.
E-mail address: secave44@gmail.com (S. Calderon V.).

0257-8972/$ – see front matter © 2013 Elsevier B.V. All rights reserved.
http://dx.doi.org/10.1016/j.surfcoat.2013.02.011

Table 1
Deposition parameters, deposition rates and chemical compositions of ZrCN and ZrCN-nAg films.

Sample	Current density (mA/cm^2)		Power (W)		Substrate holder rotation speed (rpm)	Thickness (μm)	Deposition rate (μm/h)	Grain size (nm)	Contact angle (°)	Roughness (nm)		Composition (at.%)				
	Target		Target							RMS	Ra					
	Zr–Ag	Zr	Zr–Ag	Zr								Zr	N	C	O	Ag
ZrCN	–	10	–	1000	8.0	4.5	1.78 ± 0.14	9.2	91.6 ± 2.2	40.0 ± 15.7	29.7 ± 12.7	26.0	20.4	34.5	19.0	0
ZrCNA1	3.3	6.5	230	620	8.0	3.0	1.76 ± 0.09	7.3	109.7 ± 1.8	45.1 ± 12.7	34.9 ± 11.1	27.8	22.6	35.1	11.8	2.7
ZrCNA2	3.3	6.5	230	620	4.0	3.3	1.64 ± 0.04	4.3	108.0 ± 2.3	41.5 ± 6.2	29.5 ± 5.5	27.2	25.5	35.3	9.3	2.7

distributed within the erosion zone of the target, with a Zr/Ag area ratio around 4 (80% Zr–20% Ag). The deposition system consists of two type 2 rectangular shaped unbalanced magnetrons, located in opposite vertical directions at 70 mm of a rotating substrate holder, using a closed field configuration. The current densities and power for both targets ($200 \times 100 \times 6$ mm^3) are listed in Table 1. Substrates' current densities were registered between 0.13 and 0.16 mA cm^{-2} for all samples. Further information about the system can be found elsewhere [29]. The base pressure was maintained around 6.0×10^{-4} Pa while the work pressure rose to 2.1×10^{-1} Pa after Ar, N_2 and C_2H_2 gasses were introduced. The coatings were deposited onto Si(100) and stainless steel 316L (SS316L) using a rotating substrate holder at 8 and 4 rpm in order to avoid multilayer growth and achieve homogeneous chemical and physical characteristics in the films, while the temperature and the bias voltage were kept at 100 °C and −50 V, respectively. Ar, N_2 and C_2H_2 fluxes were kept at 60 sccm, 3.5 sccm and 10 sccm, respectively. Table 1 details some deposition parameters used during this research work.

Prior to depositions, samples were ultrasonically cleaned in distilled water, 78% ethanol and acetone for 10 min. In addition, the targets were cleaned and an etching process was carried out.

Glow discharge optical emission spectroscopy (GD-OES) experiments were performed using a Jobin Yvon RF GD Profiler equipped with a 4 mm diameter anode and operating at a typical radio frequency discharge pressure of 650 Pa and a power of 40 W. X-ray energy dispersive spectrometer (EDS) was used to determine the composition of the samples, and the setup was calibrated using standard materials of known composition. Thicknesses were evaluated by the Calotest method utilizing a rotation sphere 20 mm in diameter at 1000 rpm for 90 s in order to obtain the desired wear.

Crystalline phases were evaluated by X-ray diffraction (XRD) by means of a Siemens diffractometer with Co Kα (1.78897 Å) radiation. The cross section of the films was assessed using a NanoSEM-FEI Nova 200 scanning electron microscope in order to determine the growth of the films compared with Thornton's model [30]. The surface characteristics such as roughness were estimated by atomic force microscopy.

Contact angle measurements were carried out by means of a DataPhysics OCA 20 using 2 μL of NaCl 0.89% w/v in order to evaluate the surface's ability to absorb simulated human fluid.

Electrochemical corrosion was assessed by electrochemical impedance spectroscopy and potentiodynamic anodic polarization. The tests were performed by means of a Gamry REF600 potentiostat on the bare and coated 316L stainless steels. A classic corrosion cell having a platinum counter electrode and a saturated calomel (SCE) reference electrode was used. The samples were kept in contact with the electrolyte solution (8.9 g/l NaCl) at 37 °C for 1 h to obtain a stable open circuit potential (OCP). A sinusoidal AC perturbation of 10 mV (RMS) amplitude was then applied to the electrode over the frequency range of 0.1 Hz–100 kHz. The impedance spectra were collected as a function of exposure time, at regular intervals, up to fifteen days of immersion. Finally, DC electrochemical testing as a complement for EIS measurements was performed; the potential was scanned from −300 mV vs. OCP to +1500 mV vs. OCP at 60 mV/min.

For the silver ion release tests, samples with an area of 4 cm^2 were immersed in two vessels, one containing 50 ml of HNO_3 (0.1 M) and the other 50 ml of 0.89% w/v NaCl at room temperature. 2 ml of each solution was taken at different times within a period of 30 days and reserved for inductively coupled plasma optical emission spectrometry (ICP-OES) analysis. The HNO_3 was used to prevent AgCl formation and to evaluate an accelerated stage of the process since HNO_3 could

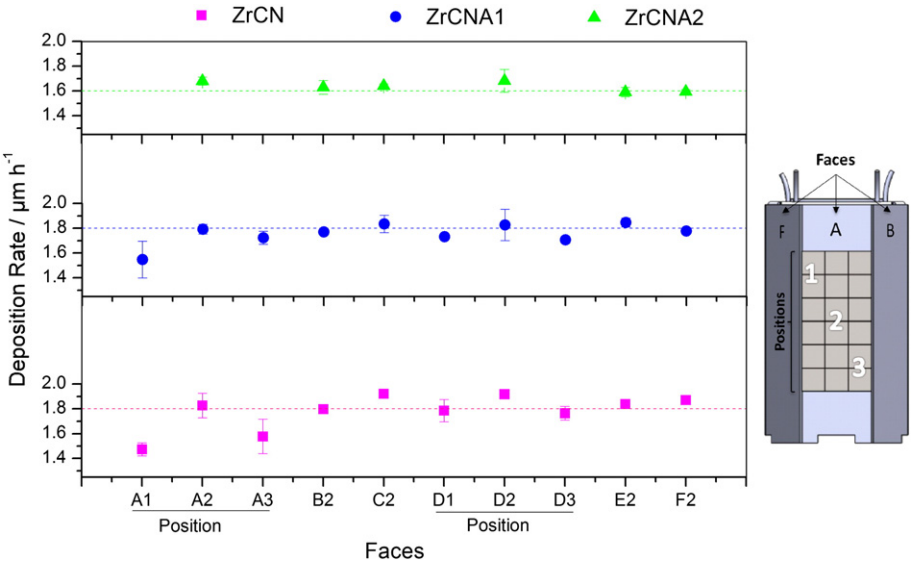

Fig. 1. Deposition rates as a function of the substrate position in the substrate holder. Inset — scheme of the substrates' position and distribution in the substrate holder.

induce $AgNO_3$ formation and produce more Ag ions. NaCl, on the other hand, was used to assess the ratio between the accelerated (HNO_3) and the non-accelerated processes. Tests were carried out using the ICP spectrometer model JY 2000 2.

Finally, taking into consideration future biological tests, which require several replicated trials, it is essential to maximize the number of substrates in every deposition. However, before performing expensive and time consuming biological tests, it is fundamental to confirm that the chemical and physical (morphology/structure) film's properties are independent of the substrate's position at the substrate holder. Therefore, the first step on this work was to evaluate the structure, thickness and profile composition of the films, taking into account the samples' positions on the substrate holder.

The inset in Fig. 1 schematizes the samples' positions on the substrate holder as it was used during each deposition.

3. Results and discussion

3.1. Physical and chemical characterization

Fig. 1 shows the deposition rate versus location in the substrate holder. The samples were placed using a matrix-like configuration, having three columns and six rows in each face. The results reveal a slight decreasing gradient of the deposition rate, related to the positions within the faces. However, the statistical analysis did not show any significant difference for the majority of the samples. The samples' location, in relation to the faces, does not influence the deposition rate since the rotation of the substrate holder allows homogeneous growth, independently of the rotation speed. However, the substrate holder rotation speed influenced the deposition rate between samples; samples deposited with a lower rotation speed present lower deposition rates, probably due to the fact that the deposition rate is found to be higher in front of the active targets and lower when the substrate moves away from the active targets, as reported by Haider and Hashmi [31]. The deposition rates calculated by an average between deposition rates from various faces and different positions in the substrate holder are presented in Table 1.

GD-OES profiles do not show any significant difference between the samples. Fig. 2 depicts the GD-OES profiles for the ZrCNA1 and ZrCNA2 samples in two different positions within the substrate holder, revealing homogeneous in-depth profile composition for all the samples. When comparing the Zr signal in different positions within the same face, for instance, a 4% increase is noticed from a position near the top of the substrate holder moving toward the center. This variation was not considered significant since it was equally noticed in the substrate, in spite of the fact that the substrate came from the same lot (Fig. 2a). On the same basis, when comparing different faces within the same position, the Zr variation was not significant (Fig. 2b). Moreover, silver shows a constant distribution throughout the film; no precipitation to the surface was found for both samples (Fig. 2a inset). These results possibly express a homogeneous environment within the chamber; therefore, further characterizations of structure, ion release behavior and corrosion resistance were carried out without taking into consideration sample position on the substrate holder.

Fig. 3 displays the XRD patterns for the deposited samples. The first sample (without Ag) exhibits two diffraction peaks at 38.5° and 45° corresponding to (111) and (200) peaks originated by a face centered cubic lattice structure, typical for a B1-NaCl crystal structure, whose positions lie intermediate between those for the bulk ZrC and ZrN phases. Considering the mutual solid solubility of the ZrC–ZrN system, which is typical for $ZrC_{1-x}N_x$ films [13,14], the formation of a $ZrC_{1-x}N_x$ phase is foreseen. A contribution to the peak shift due to compressive residual stress in the coating can also be considered. With the incorporation of silver, ZrC_xN_{1-x} diffraction peaks get broader and shift to higher angles. This shift might be explained by the addition of silver to the system and by doing so, the coatings may release some

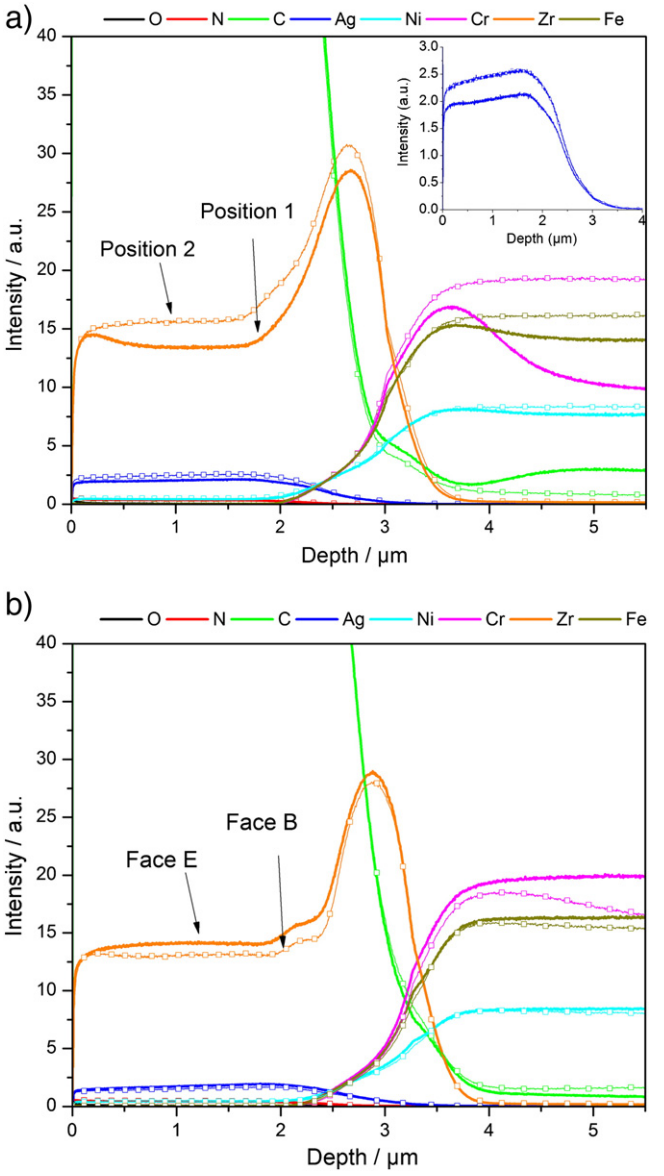

Fig. 2. GD-OES profile comparison between faces and positions within the substrate holder. (a) ZrCNA1 comparison between positions 1 and 2. (b) ZrCNA2 comparison between faces B and E. Inset — silver profile for ZrCNA1 (positions 1 and 2).

compression stress typical of coatings deposited by physical vapor deposition (PVD), due to the mixture of hard (ZrC_xN_{1-x}) and soft (Ag) phases.

Furthermore, the Scherrer formula was used to calculate the ZrC_xN_{1-x} grain size, demonstrating that by adding silver to the system, a reduction in the grain size within the structure is observed (see Table 1). This variation could be due to the simultaneous growth of Ag and ZrC_xN_{1-x} phases since the deposition of Ag causes an interrupted nucleation of the ZrC_xN_{1-x} crystals leading to smaller crystal sizes. In addition, a further and more pronounced reduction is detected by changing the substrate rotation speed, which may be due to the ion bombardment increase in the substrate holder caused by a velocity reduction of the substrate holder.

In addition, taking into account the atomic composition (Table 1), an excess of C and N is noticed over the Zr content. This can be understood by assuming the formation of carbon-based phases (a-C and a-CN_x) where atoms are connected to C or N atoms preferentially by sp^2 bonds as observed in previous publications [14].

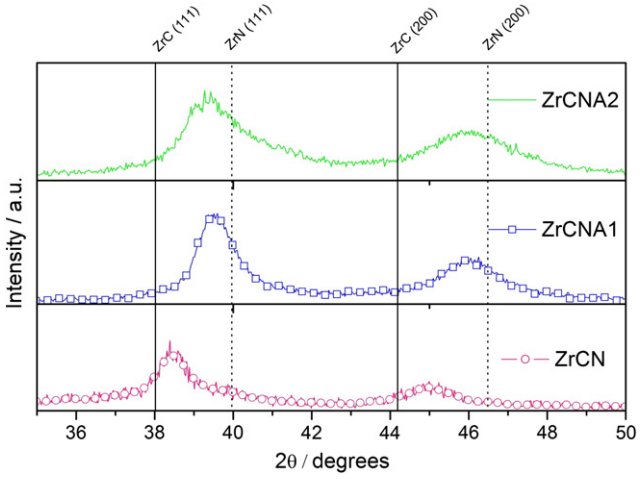

Fig. 3. XRD diffractograms of ZrCN and $ZrC_{1-x}N_x$-nAg. Peak positions obtained from the International Centre for Diffraction Data (ICDD) database for the materials ZrN (ICDD card no. 03-065-2905) and ZrC (ICDD card no. 01-074-1221) are indicated as references.

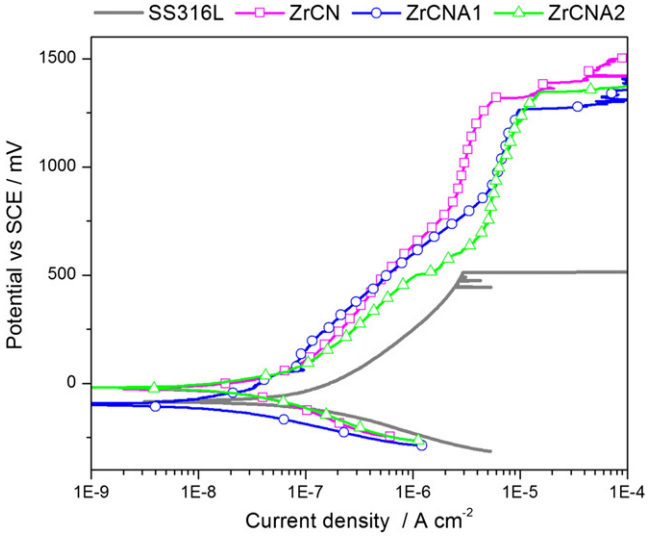

Fig. 5. Anodic polarization curves obtained for ZrCN, $ZrC_{1-x}N_x$-nAg and SS316L in 8.9 g/l NaCl electrolyte at 37 °C.

Although all films showed similar surface morphology, some differences were observed in the fractured cross sectional images (Fig. 4). The coatings on higher rotation speed exhibited a slightly higher columnar structure angle (10°) compared with films deposited at a slower rotating speed. This difference is explained by the fact that the rotation speed induces a tilt in the substrate with respect to the target position; the change in velocity leads to a variation in the incidence angle of the particles contacting the substrate, thus, since the homologous temperature (the ratio between the substrate temperature and the melting temperature of the deposited material) is very low, the adatom mobility is near zero, caused by the low energy of the particles, preventing the adatoms from overcoming the diffusion barrier [32]. SEM cross section images reveal the approximately 500 nm Zr interlayer films and the 2.8 μm $ZrC_{1-x}N_x$ coating, in agreement with the ball-cratering results (Table 1).

The growth mechanisms of the films could be framed within ZONE T of the structure zone model described by Thornton [30], mainly attributed to the low deposition temperature and high nitrogen content [14].

On the other hand, the contact angle was evaluated with the aim of correlating the films' hygroscopic properties with the coatings' corrosion resistance. Table 1 shows the contact angle obtained for all the samples. ZrCN coatings present the lowest contact angle among the films; however, all the films have higher contact angles than the substrate (85.5°), primarily due to the double-roughness surface created by the substrate grains together with the columnar growth of the films. In addition, silver introduction increases the double-roughness property of the surface triggering a rise in the contact angle.

ZrCN coatings showed a lower contact angle, also interpreted as less hygroscopic material or higher surface energy, which has been reported to influence the corrosion resistance in terms of corrosion rate and pitting corrosion potential [33]. In addition, the water/electrolyte intake is likely to increase in these types of compounds. Therefore, with a higher electrolyte intake capacity, the electrolyte could be more easily absorbed by the films and reach the substrate. As a result, and despite the fact that ZrCN films are thicker than $ZrC_{1-x}N_x$-nAg films, the corrosion behavior in all the films is equivalent, as will be discussed in the following section.

3.2. Electrochemical characterization

In Fig. 5, an overlap of the anodic polarization curves are presented for all samples. For comparison, the polarization curve of the substrate is also plotted. The graph clearly depicts that the presence of the coatings improves the corrosion properties of the stainless steel. The shift to lower current values for the coated stainless steel by almost one order of magnitude reveals such enriched corrosion behavior for those coatings. It should be stressed that structural aspects related to the amount of defects, grain size, and columnar growth of the films are expected to have some influence on this behavior [34].

In fact, the slightly better corrosion resistance observed for the ZrCNA1 film compared to ZrCNA2 might be partially attributed to the fact that the latter appears to have a decrease in grain size, inducing more grain boundaries in the system, and therefore, increasing preferential points for corrosion [35].

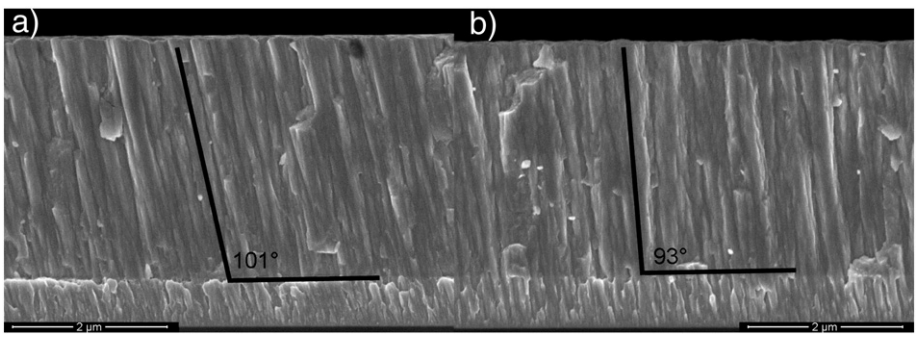

Fig. 4. SEM cross-section images of coatings synthesized at different substrate holder rotation speeds: (a) ZrCNA1 — 8 rpm, (b) ZrCNA2 — 4 rpm.

Additionally, metastable pitting was observed for the coated steel near the stainless steel breakdown potential; after this potential, a less active zone is revealed for the coated steel, showing a passive zone from the SS316L pitting potential to the breakdown potential of the films. The enhancement of the pitting potential represents the reduction of the samples' tendency to pitting and may be due to the fact that the roughness of the SS316L (70 μm) is reduced by coating it, decreasing the nucleation spots, and hence, the nucleation rate of pits, as reported by Yu Zuo et al. [36]. This breakdown potential is largely increased in the films compared to the bare stainless steel but with large standard deviations for each sample (117 mV). Hence, due to the fact that this potential is strongly related to the surface morphology of the samples, this variation may indicate the importance of more homogeneous surfaces in order to stabilize the pitting potential, and thereby, improve protection. However, since one of the major problems of SS316L is the localized corrosion, the ZrCN films exhibited protective behavior, even with the silver incorporation.

EIS analysis showed very stable films throughout the 15 days of the experiment. In Fig. 6a and b, the results of EIS tests for the films are presented, showing the Bode Z plot (frequency vs impedance modulus |Z|), as well as the Bode phase plot (frequency vs phase angle) for 0 h and 336 h of immersion, respectively. Impedance modulus reveals an increased impedance value in the entire frequency range for covered samples, implicating an enhanced corrosion behavior compared to the substrate. Nevertheless, no changes are noticed after 15 days of immersion other than the slight impedance decrease

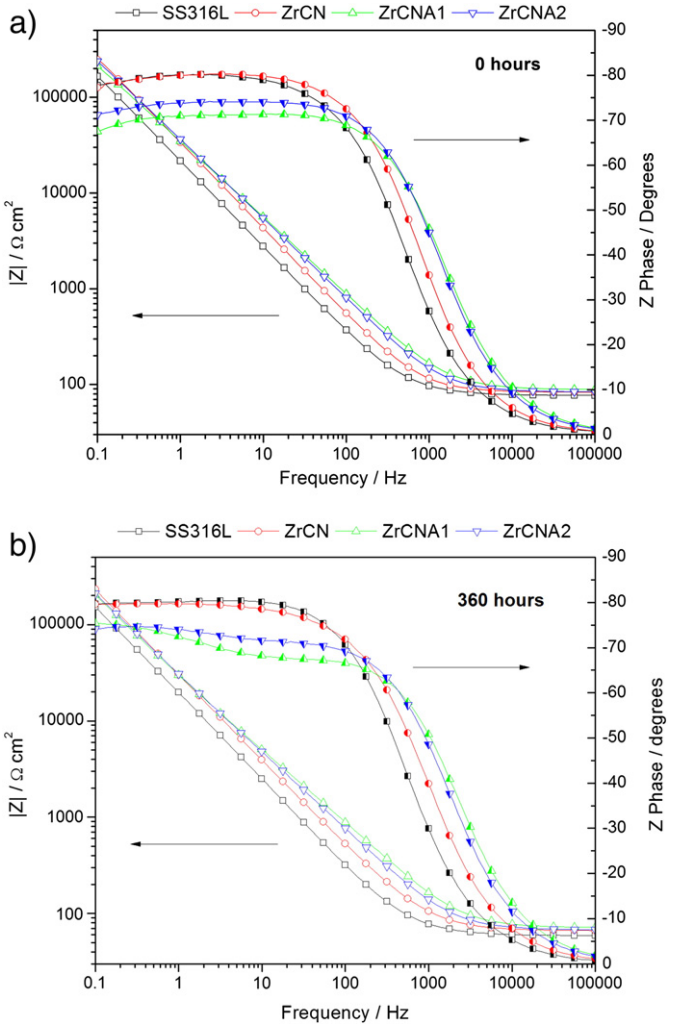

Fig. 6. Bode plot and modeling of EIS spectra: (a) 0 h of immersion; (b) 336 h of immersion.

at high frequencies, which can represent a slight change of electrolyte resistance with time. However, some differences can be noticed in the phase angle graphs (Fig. 6). Even though the log |Z| is linear with respect to the log of the frequency in all samples, revealing a predominantly capacitive behavior [37], the SS316L and ZrCN showed phase angles closer to 90°, which represent a pure capacitive response. $ZrC_{1-x}N_x$-nAg samples, on the other hand, showed a second time constant emergence after the first 24 h of exposure, which permits the differentiation of the interfaces present in the system, such as the film–substrate and film–electrolyte interfaces. Subsequently, the data have been fitted using two different equivalent circuits shown in Fig. 7.

Fig. 7a, symbolizes the equivalent circuit (EQC) used for fitting the SS316L and $ZrC_{1-x}N_x$ EIS data, where the R_{sol} represents the solution resistance, R_p denotes the charge transference resistance and CPE is the phase constant element replacing the double layer capacitance usually utilized to take into consideration the frequency dispersion observed due to surface characteristics [38]. On the other hand, two elements were added to the EQC to fit the $ZrC_{1-x}N_x$-nAg data in order to take into account the contribution of the porosity and the capacitance characteristic of the films (Fig. 7b).

In Fig. 8, the polarization resistance estimated from the EIS experiments is presented. It should be noticed that polarization resistance is an electrochemical parameter estimated from EIS results, which is inversely proportional to the corrosion rate. The polarization resistance (Fig. 8) was calculated as the sum of the pore resistance (R_{por}) and the resistance in the substrate–film interface (R_s), for the circuit type II [39] showing the highest polarization resistance for ZrCNA1, in concordance with the potentiodynamic results. This resistance revealed an increasing tendency as a function of time for all coatings, suggesting that the pores within the coating are being blocked with corrosion products; therefore, the ionic movement in the coatings was inhibited since the electric resistance of rust is greater than the solution [40,41]. In addition, AgCl is likely to be formed in the presence of Cl ions [42], being insoluble in water at 37 °C, providing an extra charge transference inhibition.

Even though the CPE capacitance (Q) is related to the coating capacitance, it is not possible to equal this parameter to the real film capacitance, and thereby, it is necessary to explore the relationship between these parameters. Brug et al. [43], for example, have proposed the relationship shown in Eq. (1), for EQC.

$$C_{eff} = Q^{\frac{1}{n}}\left(\frac{1}{R_{sol}} + \frac{1}{R_p}\right)^{\frac{n-1}{n}} \quad (1)$$

This effective capacitance has been calculated and the results are presented in Fig. 9 illustrating the tendencies of this parameter as a function of time. It may be noticed that the effective capacitance, related to the dielectric constant of the material as described in Eq. (2) [44], presents a very steady behavior during time in all films. Therefore, since the coatings show a steady capacitance behavior, it could be concluded that the films' dielectric properties remain unchanged, regardless of the silver reduction as a function of time as evidenced by ICP results.

$$C_{eff} = \frac{\varepsilon\varepsilon_0 A_c}{d} \quad (2)$$

where ε and ε_0 are the dielectric constant of the coating and the permittivity of free space, respectively, d is the coating thickness and A_c is the exposed area of the film.

3.3. Silver ion release

Fig. 10 reports the accumulative silver ions released in 8.9 g/l of NaCl and HNO_3 as a function of time. Exponential curve tendency

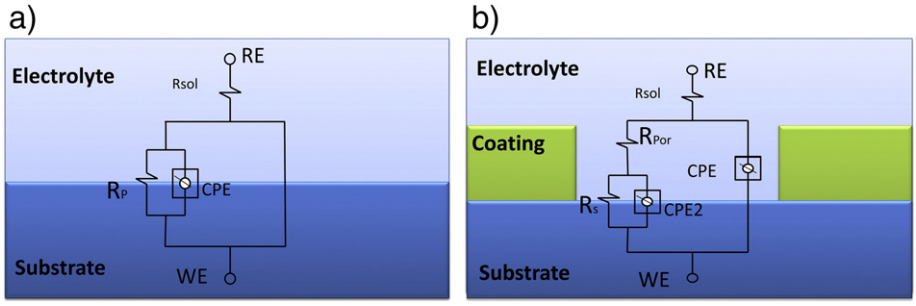

Fig. 7. Establishment of EQCs for (a) SS316L and SS316L/ZrCN; (b) SS316L/ZrCNA1 and SS316L/ZrCNA2. R_{sol} is the solution resistance, R_p denotes the charge transference resistance and CPE is the phase constant element.

was added to the graphs in order to determine the trend of the samples during time. In general, ZrCNA1 samples showed the highest Ag^+ release. Coatings immersed into nitric acid showed a higher Ag^+ release from the beginning to the end of the experiment. Furthermore, the silver ion release trend remains increasing after 30 days, in contrast to the NaCl solution which levels out after a certain time.

In the case of the samples immersed into sodium chloride, a steady stage was reached between 7 and 8 days of immersion. The silver ion release stabilization is not due to a solution saturation, since every film was immersed into 50 ml of each solution, and therefore, the saturation level of NaCl and/or HNO_3 should be equal for each solution in every sample. Hence, it is believed that the plateau-like behavior of Ag^+ is mainly due to formation of chemical compounds in the diffusion paths, reducing and/or avoiding the silver release from the inner part of the coatings, confirmed by EIS results where the coating polarization resistance increases. Two compound sources may be considered as the causes of the blocking behavior. On the one hand, the corrosion of the substrate may induce Fe, Ni and Cr ions to be released from the substrate. On the other hand, silver possibly formed AgCl since the NaCl solution is rich in Cl ions. In addition, this obstructive behavior could have been avoided in more acidic electrolytes since these compounds are more soluble at a lower pH [45,46], which explains the difference between NaCl and HNO_3 solutions.

Despite the fact that the composition, thickness, absorption capacity and silver content are similar, the structures of the ZrCNA1 and ZrCNA2 samples are different and induce a slightly different corrosion behavior, prompting a larger corrosion current for the latter mentioned films; and thereby, inducing more corrosion products such as Fe ions which block the diffusion paths with a faster ratio compared to the ratio of the ZrCNA1, which could explain the differences between silver release for both samples.

It may be stressed that the total amount of silver released to the media corresponds only to approximately 10% of the silver present in the films. This amount may correspond to the silver located on the surface of the material and on the column's boundaries. However, once this silver is ionized, the silver remains in the interior of the films in a metallic state form. As a result, 90% of the silver is maintained in the coatings and must be activated in a certain manner to continue the antibacterial effect for longer periods.

Additionally, it must be mentioned that the silver concentration reported to be antibacterial is around 32 ppb [47], reached between 16 and 25 h in all the films, a period in which bacteria may grow and form biofilm. However, the first 2 h during the immersion is determinant for antibacterial surfaces since during this stage bacteria colonization takes place; therefore, it is crucial to increase the silver ion release speed during the first hours and maintaining the release rate during a long period of time, sufficiently long to be applied in long term devices. On the other hand, the highest release values reported on this paper vary from 162 to 396 ppb, values that should be maintained below 1 to 100 ppm so that adverse reactions within the human body are not produced [47].

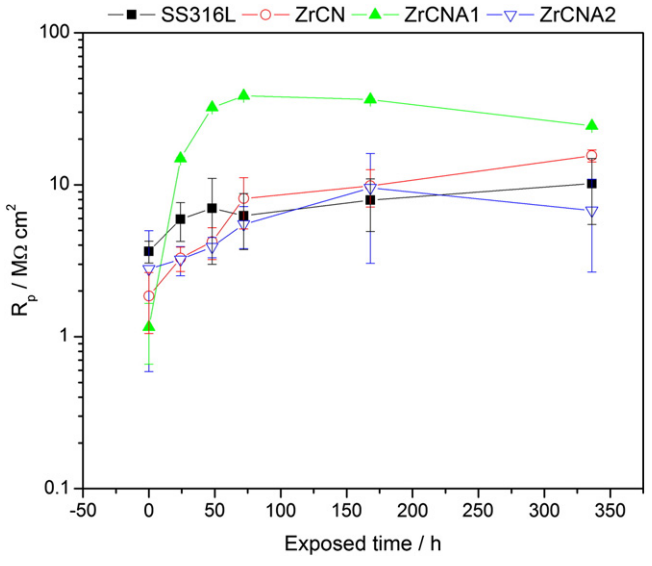

Fig. 8. Polarization resistance (R_p) as a function of immersion time estimated from EIS analysis.

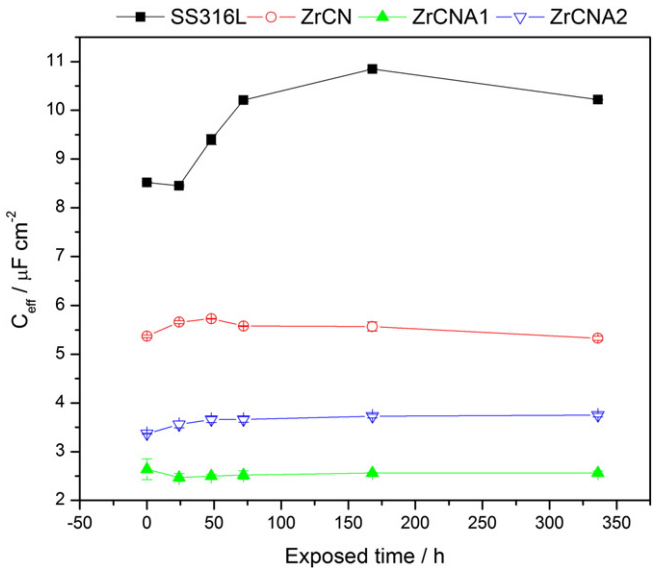

Fig. 9. Effective capacitance as a function of immersion time estimated from EIS analysis.

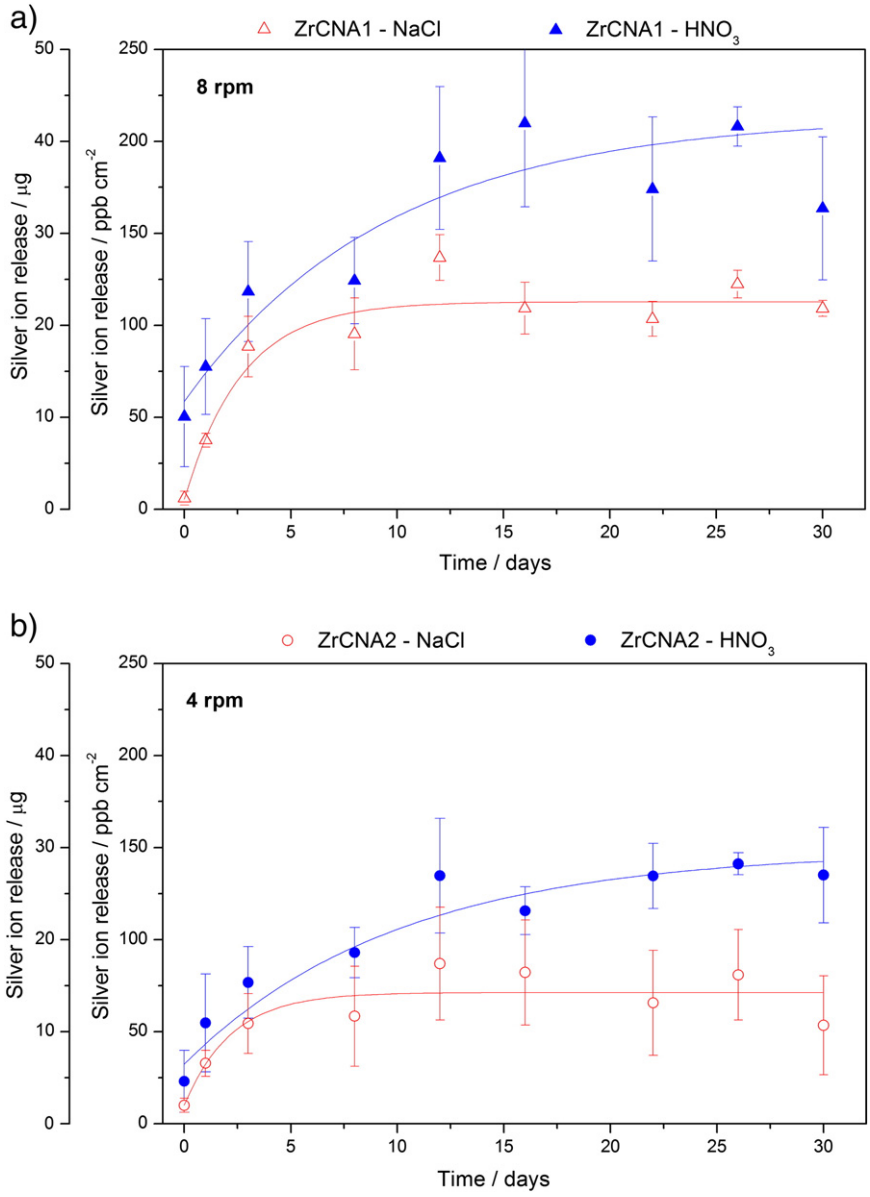

Fig. 10. Total Ag^+ release as a function of time by various $ZrC_{1-x}N_x$ coatings with changes in the structures for HNO_3 solution at 0.1 M and 8.9 g/L NaCl. (a) ZrCNA1 and (b) ZrCNA2.

4. Conclusions

$ZrC_{1-x}N_x$-nAg coatings were deposited by unbalanced magnetron sputtering. Electrochemical measurements revealed an improvement in the corrosion behavior of the coated steel compared with the bare steel. Results also showed that the silver introduction does not affect the coatings' corrosion resistance. Nonetheless, the films' microstructure has been found to play a significant role related to the films' corrosion resistance since factors such as grain size and columnar growth could reduce this property in the system. As expected, silver ion release was larger for the samples immersed into a more acidic electrolyte. Samples immersed into NaCl showed a maximum ion release between 7 and 8 days of immersion, which could be interpreted as a blocking behavior. However, samples with the same silver content showed different Ag^+ release values, leading to the deduction that the corrosion and microstructure may influence its diffusion/dissolution.

These materials could be a plausible solution for short term biomaterial applications. However, biocompatibility and antibacterial tests must be performed. Additional studies must be carried out in order to confirm the compounds inducing the silver release reduction.

Acknowledgments

The authors are grateful to 3B's Research Group in Biomaterials, Biodegradables and Biomimetics for the ICP measurements and Prof. Isabel Leonor, PhD for her assistance. This research is partially sponsored by FEDER funds through the program COMPETE—Programa Operacional Factores de Competitividade and by Portuguese national funds through FCT—Fundação para a Ciência e a Tecnologia, under the project ANTIMICROBCOAT—PTDC/CTM/102853/2008. This work has also been supported by the Ministerio de Ciencia e Innovación of Spain through the Consolider-Ingenio 2010 program (CSD2008-00023) and through the project RyC2007-0026.

References

[1] V. Saikko, Proc. Inst. Mech. Eng. H J. Eng. Med. 206 (1992) 201.
[2] M. Balaceanu, T. Petreus, V. Braic, C.N. Zoita, A. Vladescu, C.E. Cotrutz, M. Braic, Surf. Coat. Technol. 204 (2010) 2046.
[3] M. Balaceanu, V. Braic, A. Kiss, C.N. Zoita, A. Vladescu, M. Braic, I. Tudor, A. Popescu, R. Ripeanu, C. Logofatu, C.C. Negrila, Surf. Coat. Technol. 202 (2008) 3981.
[4] J.D. Gu, P.L. Chen, Surf. Coat. Technol. 200 (2006) 3341.

[5] M. Balaceanu, V. Braic, M. Braic, A. Vladescu, C.N. Zoita, C.E.A. Grigorescu, E. Grigore, R. Ripeanu, Solid State Sci. 11 (2009) 1773.
[6] M. Braic, V. Braic, M. Balaceanu, C.N. Zoita, A. Kiss, A. Vladescu, A. Popescu, R. Ripeanu, Mater. Chem. Phys. 126 (2011) 818.
[7] C.-S. Chen, C.-P. Liu, J. Non-Cryst. Solids 351 (2005) 3725.
[8] D. Craciun, G. Bourne, G. Socol, N. Stefan, G. Dorcioman, E. Lambers, V. Craciun, Appl. Surf. Sci. 12 (2011) 5332–5336.
[9] E. Grigore, C. Ruset, X. Li, H. Dong, Surf. Coat. Technol. 204 (2010) 1889.
[10] I.A. Khan, S. Jabbar, T. Hussain, M. Hassan, R. Ahmad, M. Zakaullah, R.S. Rawat, Nucl. Inst. Methods Phys. Res. B 268 (2010) 2228.
[11] F. Hollstein, D. Kitta, P. Louda, F. Pacal, J. Meinhardt, Surf. Coat. Technol. 142–144 (2001) 1063.
[12] S. Kudapa, K. Narasimhan, P. Boppana, W.C. Russell, Surf. Coat. Technol. 120–121 (1999) 259.
[13] M.M. Larijani, M.B. Zanjanbar, A. Majdabadi, J. Alloys Compd. 492 (2010) 735.
[14] E. Silva, M. Rebelo de Figueiredo, R. Franz, R. Escobar Galindo, C. Palacio, A. Espinosa, S. Calderon V, C. Mitterer, S. Carvalho, Surf. Coat. Technol. 205 (2010) 2134.
[15] O. Akhavan, E. Ghaderi, Surf. Coat. Technol. 203 (2009) 3123.
[16] K. Vasilev, V. Sah, K. Anselme, C. Ndi, M. Mateescu, B.r. Dollmann, P. Martinek, H. Ys, L. Ploux, H.J. Griesser, Nano Lett. 10 (2009) 202.
[17] R. Hauert, Diamond Relat. Mater. 12 (2003) 583.
[18] F. Marciano, L. Bonetti, L. Santos, N. Da-Silva, E. Corat, V. Trava-Airoldi, Diamond Relat. Mater. 18 (2009) 1010.
[19] N. Chekan, N. Beliauski, V. Akulich, L. Pozdniak, E. Sergeeva, A. Chernov, V. Kazbanov, V. Kulchitsky, Diamond Relat. Mater. 18 (2009) 1006.
[20] H.W. Choi, R.H. Dauskardt, S.C. Lee, K.R. Lee, K.H. Oh, Diamond Relat. Mater. 17 (2008) 252.
[21] S. Kwok, W. Zhang, G. Wan, D. McKenzie, M. Bilek, P.K. Chu, Diamond Relat. Mater. 16 (2007) 1353.
[22] R. Hauert, Diamond Relat. Mater. 12 (2003) 583.
[23] C. Hu, J. Guo, J. Qu, X. Hu, Appl. Catal. Environ. 73 (2007) 345.
[24] J. Zhao, X. Cai, H. Tang, T. Liu, H. Gu, R. Cui, J. Mater. Sci. Mater. Med. 20 (2009) 101.
[25] A. Mo, J. Liao, W. Xu, S. Xian, Y. Li, S. Bai, Appl. Surf. Sci. 255 (2008) 435.
[26] B.S. Necula, L.E. Fratila-Apachitei, S.A.J. Zaat, I. Apachitei, J. Duszczyk, Acta Biomater. 5 (2009) 3573.
[27] N. Stobie, B. Duffy, S.J. Hinder, P. McHale, D.E. McCormack, Colloids Surf. B: Biointerfaces 72 (2009) 62.
[28] R.F. Bunshah, Handbook of Hard Coatings, first ed., William Andrew Publishing, Noyes, 2001.
[29] E. Ribeiro, A. Malczyk, S. Carvalho, L. Rebouta, J.V. Fernandes, E. Alves, A.S. Miranda, Surf. Coat. Technol. 151–152 (2002) 515.
[30] J.A. Thornton, Annu. Rev. Mater. Sci. 7 (1977) 239.
[31] J. Haider, M. Hashmi, Adv. Mater. Res. 83 (2010) 977.
[32] S. Mahieu, P. Ghekiere, D. Depla, R. De Gryse, Thin Solid Films 515 (2006) 1229.
[33] Y. Wang, H. Li, Y. Zheng, S. Wei, M. Li, Appl. Phys. Lett. 96 (2010) 251909.
[34] M. Diesselberg, H.R. Stock, P. Mayr, Surf. Coat. Technol. 177–178 (2004) 399.
[35] L. Liu, Y. Li, F. Wang, Electrochim. Acta 53 (2008) 2453.
[36] Y. Zuo, H. Wang, J. Xiong, Corros. Sci. 44 (2002) 25.
[37] C. Liu, P.K. Chu, G. Lin, D. Yang, Corros. Sci. 49 (2007) 3783.
[38] C. Robyr, P. Agarwal, P. Mettraux, D. Landolt, Thin Solid Films 310 (1997) 87.
[39] D. Turcio-Ortega, S. Rodil, S. Muhl, Diamond Relat. Mater. 18 (2009) 1360.
[40] M. Behzadnasab, S.M. Mirabedini, K. Kabiri, S. Jamali, Corros. Sci. 53 (2011) 89.
[41] C. Liu, Q. Bi, A. Matthews, Corros. Sci. 43 (2001) 1953.
[42] M. Yoshinari, Y. Oda, T. Kato, K. Okuda, Biomaterials 22 (2001) 2043.
[43] G. Brug, A. Van Den Eeden, M. Sluyters-Rehbach, J. Sluyters, J. Electroanal. Chem. Interfacial Electrochem. 176 (1984) 275.
[44] C. Liu, Q. Bi, A. Leyland, A. Matthews, Corros. Sci. 45 (2003) 1257.
[45] A.G. Kim, Fuel 88 (2009) 1444.
[46] X. Shan, J.H. Payer, J. Electrochem. Soc. 156 (2009) C313.
[47] B.S. Necula, L.E. Fratila-Apachitei, S.A.J. Zaat, I. Apachitei, J. Duszczyk, Acta Biomater. 5 (2009) 3573.